

Strength of diamond beyond the elastic limit under dynamic compression

K. Katagiri^{1,2*}, N. Ozaki^{1,2}, L. E. Dresselhaus-Marais^{3,4}, J. H. Eggert³, Y. Inubushi^{5,6},
T. Irifune^{7,8}, M. Koenig^{1,9}, T. Matsuoka¹⁰, K. Miyanishi⁶, H. Nakamura¹,
N. Nishiyama¹¹, T. Okuchi¹², T. Sekine^{1,13}, Y. Seto¹⁴, K. Sueda⁶, Y. Tange⁵,
T. Togashi^{5,6}, Y. Umeda¹², M. Yabashi^{5,6}, T. Yabuuchi^{5,6}, and R. Kodama^{1,2}

¹Graduate School of Engineering, Osaka University, Osaka 565-0871, Japan.

²Institute of Laser Engineering, Osaka University, Osaka 565-0871, Japan.

³Lawrence Livermore National Laboratory; Livermore, CA 94550, USA.

⁴Department of MSE, Stanford University; Stanford, CA 94305, USA

⁵Japan Synchrotron Radiation Research Institute; Hyogo 679-5198, Japan.

⁶RIKEN SPring-8 Center; Hyogo 679-5148, Japan.

⁷Geodynamics Research Center, Ehime University; Ehime 790-0826, Japan.

⁸Earth-Life Science Institute, Tokyo Institute of Technology; Tokyo 145-0061, Japan.

⁹LULI, CNRS, CEA, École Polytechnique, UPMC, Univ Paris 06: Sorbonne Universités, Institut Polytechnique de Paris; 91128 Palaiseau cedex, France.

¹⁰Open and Transdisciplinary Research Initiatives, Osaka University; Osaka 565-0871, Japan.

¹¹Laboratory for Materials and Structures, Tokyo Institute of Technology; Kanagawa 226-8503, Japan.

¹²Institute for Integrated Radiation and Nuclear Science, Kyoto University; Osaka 590-0494, Japan.

¹³Center for High-Pressure Science and Technology Advanced Research; Shanghai 201203, China.

¹⁴Graduate School of Science, Kobe University; Hyogo 657-0013, Japan.

*Corresponding author. Email: kkatagiri@ef.eie.eng.osaka-u.ac.jp

Extremely high pressures over a million of atmospheres are required to deform diamonds permanently. Under dynamic high-pressure conditions, even such strong materials lose their strengths so rapidly that the initially pristine lattice transforms into complex dynamics. Here, we report femtosecond x-ray diffraction observations that directly resolve how shock waves deform the crystal lattice in the isotropic nano-polycrystalline form of diamond. The results show that the nano-grain reinforced diamond retains its strength at shock pressures far beyond its elastic limit until it finally approaches zero at 707 GPa, indicating the existence of brittle-ductile transition of nano-polycrystalline diamond under high-strain rate shock compression. The atomic-level deformation process of the diamond observed in this study is a key benchmark for designing high strength materials and simulating their behavior under extreme conditions.

Strength is one of the most critical parameters of solids. The threshold shock stress of reversible deformation (*i.e.*, Hugoniot elastic limit) has been determined as a scale of material strength at some of the fastest rates, during shock compression [1]. When a high-amplitude shock pressure exceeding the elastic limit is applied, the material quickly relieves shear stress through a transient process from a one-dimensional (1D), elastic deformation state to a three-dimensional (3D), plastic deformation [2]. This process is highly complex depending on the material and thus elucidating the elastic-plastic transition has been a long-standing goal that spans shock physics [3], materials science [4], planetary science [5,6], and high energy density physics [7,8], having yet to be fully achieved. Conventional velocity measurements provide only macroscopic and 1D views of shock deformations [9], while the pathway of the 3D deformations in the crystal lattice behind the shock wavefront remains unknown.

A fine-grained polycrystalline bulk material exhibits completely different mechanical properties than a single crystal, even if they are the same material [10,11]. In diamond, it has been reported that bulk nanopolycrystalline diamond (NPD) has the highest Vickers hardness [12] and Hugoniot elastic limit [13]. Understanding how nanograins deform against one of the highest strain-rate compression is important to design high-strength materials and using them in technology that requires extreme environments. Here, we show results of *in-situ* x-ray diffraction (XRD) measurements of laser-shocked NPD which gives insights into the understandings of elastic-plastic transition dynamics and strength evolution of the nano-grain reinforced material under shock compression.

Results

Performed at SPring-8 Angstrom Compact Free Electron Laser (SACLA), our

experiments combined laser-shock compression with *in-situ* femtosecond XRD using an x-ray free electron laser (XFEL) beam [14] to observe the deformation processes in crystals at the lattice level (Fig. 1). We launched a high strain-rate ($\sim 10^9 \text{ s}^{-1}$) shock wave into NPD samples using a high-intensity ($\sim 10^{12} \text{ W/cm}^2$) optical laser [15]. The NPD samples used in this work were synthesized by using a multi-anvil press and the initial material density was $3514 (\pm 3) \text{ kg/m}^3$. Since NPD is homogeneous and isotropic diamond with an average grain size of 10-20 nm [12], it is an ideal material to resolve how grain-reinforced materials lose their strength under shock compressions. As illustrated in Fig. 1, we define the x -axis as the shock propagation direction (normal to the sample surface) and refer to the transverse directions along the y - and z -axis as the \perp -axes since they behaved equivalently in our shock configuration. We probed the compressed states in the sample with an ultrafast (< 10 -fs duration) XFEL pulse [16] approximately 1 ns after the shock wave breaks into the NPD from the polypropylene ablator. This time delay minimized stress gradients in our samples. Our *in-situ* XRD experiments directly measured the lattice strains as the shock propagated through the NPD, resolving the shock-normal and -transverse lattice strains from both the elastic and plastic compressions (See Methods). For NPD, the longitudinal sound speed ($\sim 18 \text{ }\mu\text{m/ns}$) is much faster than the bulk sound speed ($\sim 11 \text{ }\mu\text{m/ns}$) [17], so the material supports a two-wave (elastic and plastic) shock structure.

The *in-situ* XRD patterns in Fig. 2 were observed at the different stages of the deformation with increasing shock pressure. As the diamond grains (10-20 nm) are much smaller than the size of the focused x-ray beam ($30 \times 50 \text{ }\mu\text{m}^2$), the diffraction pattern appears as smooth Debye-Scherrer rings. Because the XFEL irradiates the sample before the shock wave reaches its rear surface, the diffraction rings from the uncompressed

region of the NPD sample also appear in all the obtained XRD patterns, providing a reference for the deformations that calibrates the deformed lattice's spacing to quantify the absolute strains. The 2θ (scattering angle) - ϕ (azimuthal angle) plots and line profiles shown in Fig. 2 are corrected for the polarization factor [18] to eliminate the geometric intensity variations caused by the horizontal polarization of the x-ray beam at SACLA [16]. As the sample's inclination and associated shock propagation direction varied slightly between samples, the azimuthal angle was defined individually for each dataset based on the center for that run (see the Supplementary Information for more information). Two different photon-energies of x-ray pulses were used for different experiments in this work, causing the diffraction peaks from identical crystal planes to appear at different 2θ . Two shots recorded pure elastic deformations (measured at 11.0 keV, $\lambda = 1.127 \text{ \AA}$), while three others observed continuous elastic-plastic deformations or a single plastic deformation (measured at 10.0 keV, $\lambda = 1.240 \text{ \AA}$). The XFEL beam contained $\sim 10^{11}$ photons/pulse for both 10.0 and 11.0 keV x-ray pulses.

The longitudinal stress in the elastic deformation (σ_x) and the peak pressure in the plastic deformation (P_{max}) of NPD were estimated from the XRD-measured densities using the previously reported Hugoniot equation state of NPD under shock compression [13]. The XRD patterns shown in Fig. 2 demonstrate three different regimes of shock behavior with increasing shock pressure. At the lowest peak stresses, we observe only a single purely elastic response in the NPD that corresponds to a longitudinal elastic stress ($\sigma_x = 36$ and 92 GPa for Figs. 2a and 2b, respectively) lower than the Hugoniot elastic limit of NPD ($208 \pm 14 \text{ GPa}$) [13]. For higher peak pressures, we observed diffractions from both elastically and plastically deformed volumes, indicating that a two-wave structure forms ($P_{max} = 262$ and 388 GPa for Figs. 2c and 2d, respectively). At an even

higher pressure of $P_{max} = 707$ GPa, we only observed diffractions from a plastically deformed volume (Fig. 2e). This result suggests that the elastic wave is overtaken by the subsequent plastic wave, as the plastic shock wave is nearly as fast as, if not faster than, the preceding elastic shock wave over this pressure range. Besides, this result confirms that the diamond structure is stable at shock pressures of at least up to 707 GPa, consistent with previous first principal calculation results [7].

To quantitatively evaluate the observed deformation anisotropies, we calculated lattice strain $\varepsilon = \Delta d_{hkl}/d_{0,hkl}$ in the longitudinal and transverse directions based on the observed diffraction peaks, where $d_{0,hkl}$ is the undeformed lattice spacing along the hkl plane and Δd_{hkl} is the change in d -spacing of that plane due to deformation. A full description of the strain evaluation procedure and the table listing the values of 2θ , ϕ , ε_x , and ε_{\perp} determined in this work are included in the Supplementary Information. Figure 3 shows the obtained relationship between the longitudinal strain (ε_x) and transverse strain (ε_{\perp}). From the measured strains, we determined the density ρ using the following equation: $\rho = \rho_0/[(1 - \varepsilon_x)(1 - \varepsilon_{\perp})^2]$, where ρ_0 is the density before compression. We used the Hugoniot equation of state that defines the relationship between state variables for shocked materials, as was measured for NPD by velocimetries [13], to relate our measured strains to the longitudinal stress (σ_x) in the elastic deformation and the peak pressure (P_{max}) in the plastic deformation.

From the obtained strains, we estimate the strength t of shocked NPD by assuming no shear components. This assumption allowed us to calculate strength by $t = [C_{11}(\rho) - C_{12}(\rho)](\varepsilon_x - \varepsilon_{\perp})$, where C_{ij} are the elastic constants that describe diamond's compressibility along each crystallographic axis [19]. Fig. 4 shows our measured strength for NPD along with the strength of laser-shocked micro-polycrystalline diamond

measured by using *in-situ* XRD by MacDonald *et al.* [20]. Our results show better accuracy to be compared to the previous micro-polycrystalline data due to the smaller grain size of our sample to be compared to theirs (1-10 μm) and having higher $\chi = 30^\circ$ to be compared to theirs $\chi = 110^\circ$. The strengths of laser-shocked single-crystal diamond with three different orientations obtained by using velocimetry by McWilliams *et al.* [9] are also plotted in Fig. 4. Our results indicate that the strength in laser-shocked NPD is higher than those in single-crystal and micro-polycrystalline diamond, which is thought to be the effect of grain boundary strengthening [4,13]. Additionally, while the uncertainties of these previous studies are not small enough to conclude whether plastically deformed diamond retains its strength, our experimental results with higher accuracy clearly show that some of the high strength of NPD is retained in the plastically deformed volume.

Discussion

Our XRD analysis reveals two key phenomena that link crystallographically. Starting in the elastic wave, the randomly oriented nanogranular sample elastically compresses to a range of strained states that strongly depend on the ϕ angle. The data in Fig. 2 show this as a curved XRD line in the middle column, showing the continuous orientational preference of the deformability of the material. While the deformability is clearly anisotropic in the elastic compression, no texture evolution is confirmed during this stage, as shown by the uniform diffraction intensity distributions. By contrast, the plastic wave shows a nearly opposite situation as the crystal's deformability is much closer to isotropic but significant orientational preference arises (i.e., the plastically deformed volume shows stronger signal diffracted to $\phi = \pm 40^\circ$ than at $\phi = 0^\circ$). This indicates that the initial

randomly oriented nano-grains of NPD rotate into a specific preferred orientation during plastic deformation under strong compression, a phenomenon known as “crystal texture” [21,22].

Although some brittle materials, like quartz, are known to exhibit a sudden loss of strength under shock compression as soon as the applied stress exceeds the Hugoniot elastic limit [23,24], other brittle materials are found to exhibit loss of brittleness, leading to a brittle-ductile transition under shock compression [25]. The choice of brittle or ductile under shock remains unclear for diamond [9,20] but our XRD results indicate that significant strength of NPD persists even under stresses far beyond the elastic limit, meaning NPD shows some ductility against shock compression. The control of brittle or ductile response under high pressure is thought to be made by the material’s capability to locally accommodate shear forces in different macroscopic directions [26]. Our results indicate that the grain boundaries around nanograins of diamond significantly enhance its ability to accommodate shear locally. The strength of shocked NPD in the plastically deformed volume persists until the plastic wave becomes faster than the elastic wave, overtaking it to form a single shock wave that instantaneously compresses the material directly to its peak pressure. These overtaken conditions indicate the strength in the plastic volume observed at lower pressures might be a remnant of the strength in the preceding elastic volume.

In summary, we accurately measured the anisotropy and strength of shocked nanopolycrystalline diamond to resolve how shock waves push the hardest material to fail in nanoseconds. Our femtosecond x-ray diffraction measurements revealed that the strength in NPD persists even in the plastically deformed volume, revealing a new complexity of the elastic-plastic deformation dynamics. These understandings are key to

define all material disturbances in high-energy density physics [27,28], as the anisotropy of deformation would lead the material to exhibit different physical properties under pressure [29].

Methods

Sample preparations and *In-situ* XRD measurements

The NPD samples used in this work were synthesized by using a multi-anvil press at the Geodynamics Research Center, Ehime University. The initial material density was $3514 (\pm 3) \text{ kg/m}^3$, with an average grain size of 10-20 nm [12]. A 15- μm thick polypropylene film was glued on the NPD samples and was used as the ablator material to produce a single shock front, while minimizing any emissions of hard x-rays. Our experiments used an XFEL and a high-intensity nanosecond drive laser at BL3 of SACLA [16]. We estimate the drive laser intensities to be 0.3-15 TW/cm^2 on target, based on our measured laser energies. Only for the shots with a longitudinal elastic stress of 36 (Fig. 2a) or 92 GPa (Fig. 2b), we used a phase plate (80 mm in diameter) to smooth the spatial mode of the drive laser pulse. Our delay times between the drive laser and XFEL probe pulses were tuned to probe the material within $\sim 1 \text{ ns}$ of the shock wave entering the NPD sample from polypropylene ablator; this time delay minimized stress gradients in our samples. Our experiment probed the entire sample depth.

Since the x-ray beam of SACLA is polarized horizontally, the intensity distribution of diffracted x-rays has some dependence in azimuthal angle (φ) [18] which prevents the accurate determination of the intensity distribution of XRD caused by the sample orientation. Since the polarization factors for unpolarized x-ray beam $P_{unpolarized}(2\theta)$ and for linearly polarized x-ray beam $P_{polarized}(2\theta, \varphi)$ are expressed as

$$P_{unpolarized}(2\theta) = \frac{1 + \cos(2\theta)}{2} \quad (1)$$

$$P_{polarized}(2\theta, \varphi) = \sin^2\varphi + \cos^2\varphi \cos^2(2\theta), \quad (2)$$

we can virtually obtain the intensity distribution using the unpolarized x-ray beams $I_{con}(2\theta, \varphi)$ (i.e. convert to the Bragg-Brentano geometry) from the intensity distribution of the obtained XRD data $I_{obs}(2\theta, \varphi)$ by using the following equation;

$$I_{con}(2\theta, \varphi) = \frac{1}{2} \frac{1 + \cos(2\theta)}{\sin^2\varphi + \cos^2\varphi \cos^2(2\theta)} I_{obs}(2\theta, \varphi). \quad (3)$$

The intensity distributions of the $2\theta - \varphi$ plots and 1-dimentional profiles shown in Fig. 2 have been converted to the unpolarized mode by using the equation above.

Strain determination

The azimuthal angle of the center where the distortion of the observed diffraction pattern is symmetrical is individually defined (termed as ϕ_s) for both elastic and plastic deformations in each shot data (See Supplemental Information for more information). We evaluated normal and transverse strains in NPD by assuming that ϕ_s is the direction

normal to the shock.

To quantitatively evaluate the anisotropies, we fitted the recorded diffraction peaks by Gaussian or split-Gaussian (same height but different width between the left half and the right half) to obtain the lattice spacing d_{hkl} and its errors (full width at half maximum). Then, we quantify the anisotropy of the deformations by computing lattice strain $\varepsilon = \Delta d_{hkl}/d_{0,hkl}$ in the longitudinal and transverse directions (ε_x and ε_\perp , respectively). The ε_x is determined from the scattering angle 2θ measured at the azimuthal angle of $\phi = \phi_s$ by using Bragg's law: $2d\sin\theta = n\lambda$ where n is the diffraction order. Then the ε_\perp is determined by using the equation proposed by Higginbotham and McGonegle that define the ϕ dependence of 2θ [30,31];

$$\begin{aligned} \frac{\lambda^2}{d_0^2} = & [(1 + \varepsilon_\perp)^2(\cos^2\chi\cos^2\phi + \sin^2\phi) + (1 + \varepsilon_x)^2\sin^2\chi\cos^2\phi]\sin^2 2\theta \\ & + 2\cos\chi\sin\chi[(1 + \varepsilon_x)^2 - (1 + \varepsilon_\perp)^2]\cos\phi\sin 2\theta(\cos 2\theta - 1) \quad (4) \\ & + [(1 + \varepsilon_\perp)^2\sin^2\chi + (1 + \varepsilon_x)^2\cos^2\chi](\cos 2\theta - 1)^2, \end{aligned}$$

where λ is the wavelength of the x-ray pulse, d_0 is the lattice spacing of the uncompressed sample, and χ is the rotation of the target relative to the x-ray incident angle which is 110° in our experiment. This approach showed the large shear strain components can be calculated from the observed Debye-Scherrer diffraction pattern by applying the Voigt limit, which assumes constant strain across grain boundaries [30,31]. We assume the Voigt limit for the present study, as it makes the strain calculations simpler than assuming the Reuss limit which assumes constant stress across grain boundaries. We note that the MD simulations of shock compressed diamond [19] suggested that the difference in XRD results by assuming Voigt limit and Reuss limit are smaller than our experimental error. The transverse lattice strains (ε_\perp) was determined by solving equation (4) with longitudinal lattice strains (ε_x) measured at $\phi = \phi_s$ and the 2θ collected at several

different azimuthal angles of $\phi = \phi_s \pm 5n$ degrees (n is a positive integer from 1 to 9). The strains shown in Fig. 3 are determined from the diffractions from (111) planes of shocked NPD. The ε_{\perp} shown in Fig. 3 are obtained by taking the weighted averages of transverse strains obtained at different ϕ and the uncertainties include its standard deviations.

Estimating Stresses and Pressures

The longitudinal stress in the elastic deformation (σ_x) and the peak pressure (P_{max}) in the inelastic deformation of NPD were estimated from the XRD-measured densities using the previously reported stress (longitudinal pressure) - density relationships of NPD under shock compression (known as Hugoniot) [13]. The samples from the same supplier as presenting work were used in the Hugoniot measurements reported in Ref. 13.

Data availability

The raw data generated during the x-ray diffraction experiments are available from the corresponding author on reasonable request.

References

1. Meyers, M. A. *Dynamic behavior of materials* (Wiley, New York, 1994).
2. Johnson, Q., Mitchell, A. & Evans, L. X-ray diffraction evidence for crystalline order and isotropic compression during the shock-wave process. *Nature* **231**, 310-311 (1971).

3. Zhakhovsky, V. V., Budzevich, M. M., Inogamov, N. A., Oleynik, I. I. & White, C. T. Two-zone elastic-plastic single shock waves in solids. *Phys. Rev. Lett.* **107**, 135502 (2011).
4. Bringa, E. M. et al. Ultrahigh strength in nanocrystalline materials under shock loading. *Science* **309**, 1838 (2005).
5. McWilliams, R. S. et al. Phase transformations and metallization of magnesium oxide at high pressure and temperature. *Science* **338**, 1330-1333 (2012).
6. Millot, M. et al., Shock compression of stishovite and melting of silica at planetary interior conditions. *Science* **347**, 418-420 (2015).
7. Knudson, M. D., Desjarlais, M. P. & Dolan, D. H. Shock wave exploration of the high-pressure phases of carbon. *Science* **322**, 1822 (2008).
8. Smith, R.F. et al., Ramp compression of diamond to five terapascals. *Nature*, **511**, 330-333 (2014).
9. McWilliams, R. S. et al. Strength effects in diamond under shock compression from 0.1 to 1 TPa. *Phys. Rev. B* **81**, 014111 (2010).
10. Meyers, M. A. & Chawla, K. K. *Mechanical behavior of materials* (Prentice-Hall, Upper Saddle River, NJ, 1999).
11. Madec, R. et al., The role of collinear interaction in dislocation-induced hardening. *Science* **301**, 1879 (2003).
12. Irifune, T. et al. Ultrahard polycrystalline diamond from graphite. *Nature* **421**, 599-600 (2003).
13. Katagiri, K. et al. Shock response of full density nanopolycrystalline diamond. *Phys. Rev. Lett.* **125**, 185701 (2020).
14. Ishikawa, T. et al. A compact X-ray free-electron laser emitting in the sub-ångström region. *Nat. Photonics* **22**, 540-544 (2012).
15. Swift, D. C., Tierney IV, T. E., Kopp, R. A. & Gammel, J. T. Shock pressures induced in condensed matter by laser ablation. *Phys. Rev. E* **69**, 036406 (2004).
16. Inubushi, Y. et al. Development of an experimental platform for combinative use of an XFEL and a high-power nanosecond laser. *Appl. Sci.* **10**, 2224 (2020).
17. Chang, Y. -Y., Jacobson, S. D., Kimura, M., Irifune, T. & Ohno, I. Elastic properties of transparent nano-polycrystalline diamond measured by GHz-ultrasonic interferometry and resonant sphere methods. *Phys. Earth Planet. Inter.* **228**, 47 (2014).
18. Eggert, J. H., Weck, G., Loubeyre, P. & Mezouar, M. Quantitative structure factor and density measurements of high-pressure fluids in diamond anvil cells by x-ray diffraction: Argon and water. *Phys. Rev. B* **65**, 174105 (2002).

19. MacDonald, M. J. et al. Calculation of Debye-Scherrer diffraction patterns from highly stressed polycrystalline materials. *J. Appl. Phys.* **119**, 215902 (2016).
20. MacDonald, M. J. et al. Using simultaneous x-ray diffraction and velocity interferometry to determine material strength in shock-compressed diamond. *Appl. Phys. Lett.* **116**, 23104 (2020).
21. Kocks, U. F., Tomé, C. N. & Wenk, H.-R. *Texture and anisotropy: preferred orientations in polycrystals and their effect on materials properties* (Cambridge Univ. Press, New York, 1998).
22. Margulies, L., Winther, G. & Poulsen, H. F. In situ measurement of grain rotation during deformation of polycrystals. *Science* **291**, 2392 (2001).
23. Grady, D. E. Shock deformation of brittle solids. *J. Geophys. Res.* **85**, 913-924 (1980).
24. Graham, R. A. & Brooks, W. P. Shock-wave compression of sapphire from 15 to 420 kbar. The effects of large anisotropic compressions. *J. Phys. Chem. Solids*, **32**, 2311-2330 (1971).
25. Bavdekar, S. & Subhash, G. Comparison of pressure-sensitive strength models for ceramics under ultrahigh confinement. *Int. J. Impact Eng.* **118**, 60-66 (2018).
26. Kanel, G. I., Razorenov, S. V., & Fortov, E. *Shock-wave phenomena and the properties of condensed matter* (Springer-Verlag, New York, 2004).
27. Lazicki, A. et al., Metastability of diamond ramp-compressed to 2 terapascals. *Nature* **589**, 532-535 (2021).
28. Park, H.-S. et al., Techniques for studying materials under extreme states of high energy density compression. *Phys. Plasmas* **28**, 060901 (2021).
29. Katagiri, K. et al. Optical properties of shock-compressed diamond up to 550 GPa. *Phys. Rev. B* **101**, 184106 (2020).
30. Higginbotham, A. & McGonegle, D. Prediction of Debye-Scherrer diffraction patterns in arbitrarily strained samples. *J. Appl. Phys.* **115**, 174906 (2014).
31. Singh, A. K., The lattice strains in a specimen (cubic system) compressed nonhydrostatically in an opposed anvil device. *J. Appl. Phys.* **73**, 4278 (1993).

Acknowledgements

We thank T. Shinmei of GRC for the synthesis of NPD. The experiments were performed at BL3 of SACLA with the approval of the Japan Synchrotron Radiation Research Institute (proposal nos. 2019A8041 & 2018B8069). The part of NPD sample

fabrication was conducted under the support of Joint Research Center PRIUS (Ehime University, Japan). This work was supported by grants from MEXT Quantum Leap Flagship Program (MEXT Q-LEAP) Grant No. JPMXS0118067246, Japan Society for the Promotion of Science (JSPS) KAKENHI (Grants Nos. 21J10604, 19K21866, & 16H02246), Genesis Research Institute, Inc. (Konpon-ken, Toyota), Yamada Science Foundation, and the U.S. Department of Energy by Lawrence Livermore National Laboratory under Contract DE-AC52-07NA27344. The discussion and the manuscript preparation were partially supported by HPSTAR. The high-power drive laser installed in SACLA EH5 was developed with the corporation of Hamamatsu Photonics. The installation of a Diffractive Optical Elements (DOE) to improve the smoothness of the drive laser pattern was supported by the SACLA Basic Development Program.

Author contributions

K.K and N.O. conceived the project. T.I. and N.N. prepared the NPD samples. K.K. designed and manufactured the targets. K.K., N.O., L.E.D.M., Y.I., T.M., K.M., H.N., N.N., Y.S., K.S., Y.T., T.T., Y.U., M.Y. and T.Y. conducted the experiments. K.K., N.O. analyzed the data using software developed by Y.S.. K.K., N.O. and L.E.D.M. wrote the manuscript. All authors discussed the results and commented on the manuscript.

Competing interests

The authors declare no competing interests.

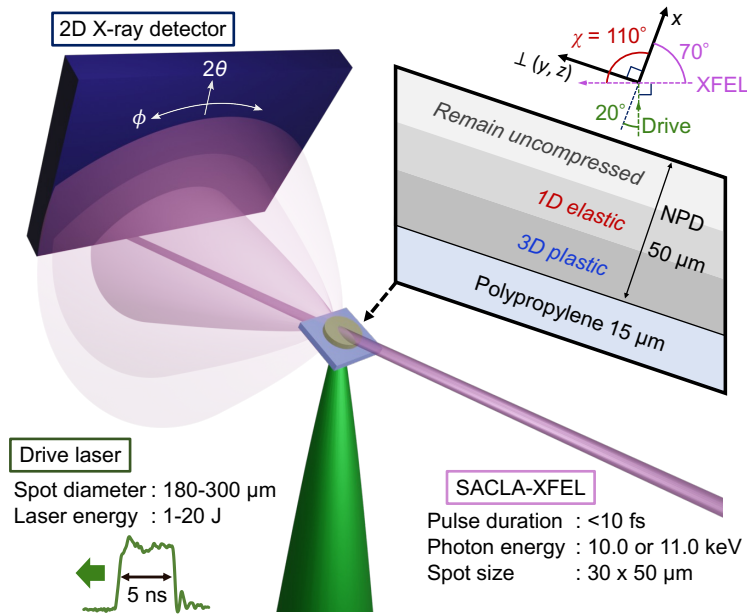


Fig. 1 | Experimental configuration. We define x as the shock wave propagation direction and \perp as the transverse direction. The angle of the shock loading direction with respect to the incident angle of the XFEL beam is $\chi = 110^\circ$ in our scheme. The first, elastic, shock wave causes the deformation uniaxially along the shock direction (x) at stress (σ_x) with little transverse stress (σ_\perp), and the second, plastic, shock wave compresses the uniaxially deformed nanograins more hydrostatically. Figures not drawn to scale.

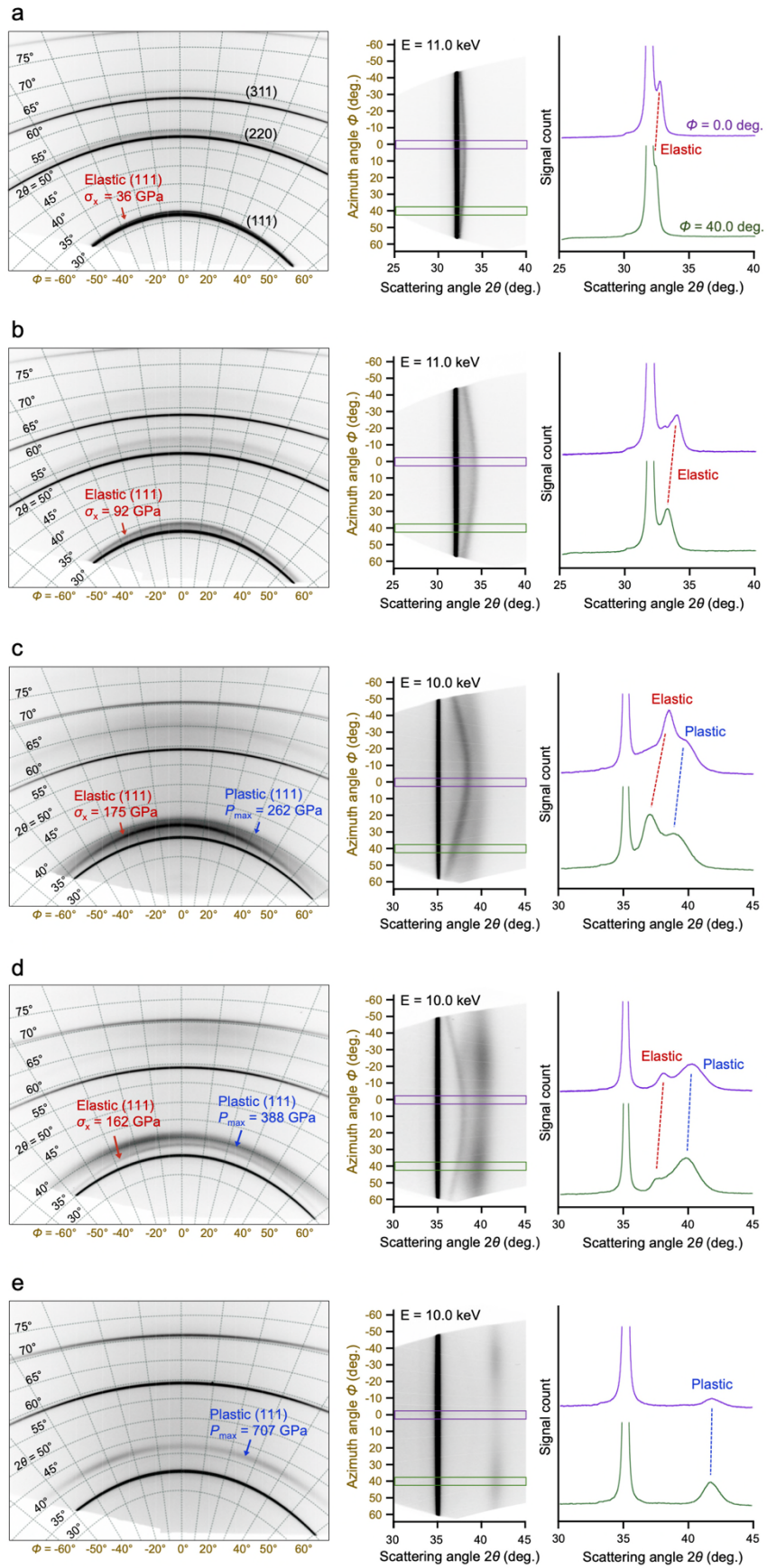


Fig. 2 | X-ray diffraction results of shock-compressed NPD. Raw diffraction images, 2θ - ϕ plots, and line profiles for (111) planes taken at $\phi = 0.0$ (purple) and $\phi = 40.0$ (green) degrees, recorded at 5 different shock pressures. The polarization factor is not corrected for the raw images, while it is corrected for the 2θ - ϕ plots and the line profiles. Dotted curves and lines shown in the raw diffraction images indicate constant scattering angle (2θ) and azimuth angle (ϕ), respectively. **a** The XRD results showing purely elastic deformation of NPD at $\sigma_x = 36$ GPa. **b** Purely elastic deformation with a higher stress of $\sigma_x = 92$ GPa. **c** Two-wave elastic-plastic deformation at $P_{max} = 262$ GPa. **d** Two-wave elastic-plastic deformation with a higher peak pressure of $P_{max} = 388$ GPa. **e** The XRD pattern showing only plastic deformation at $P_{max} = 707$ GPa.

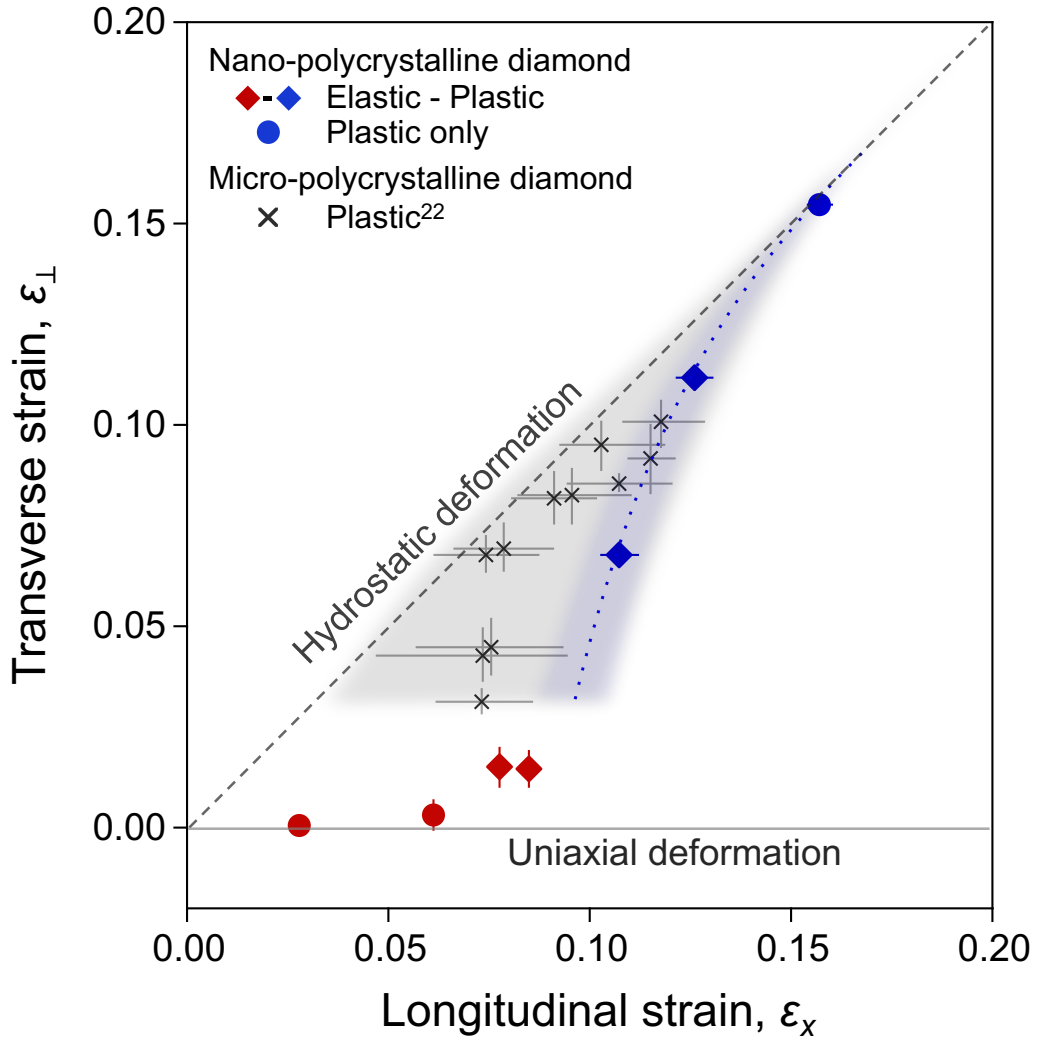


Fig. 3 | Evolution of longitudinal and transverse strains in shock compressed diamond. The red and blue circles represent the purely elastic responses and the purely plastic response of shocked NPD, respectively. The red and blue diamond-shape symbols represent the responses of continuous elastic (red) - plastic (blue) deformations of NPD. Black crosses are the plastic deformation data of micro-polycrystalline diamond from Ref. 22. Blue and grey shaded areas and blue dotted curve are guides to the eyes to highlight the difference between NPD and micro-polycrystalline diamond.

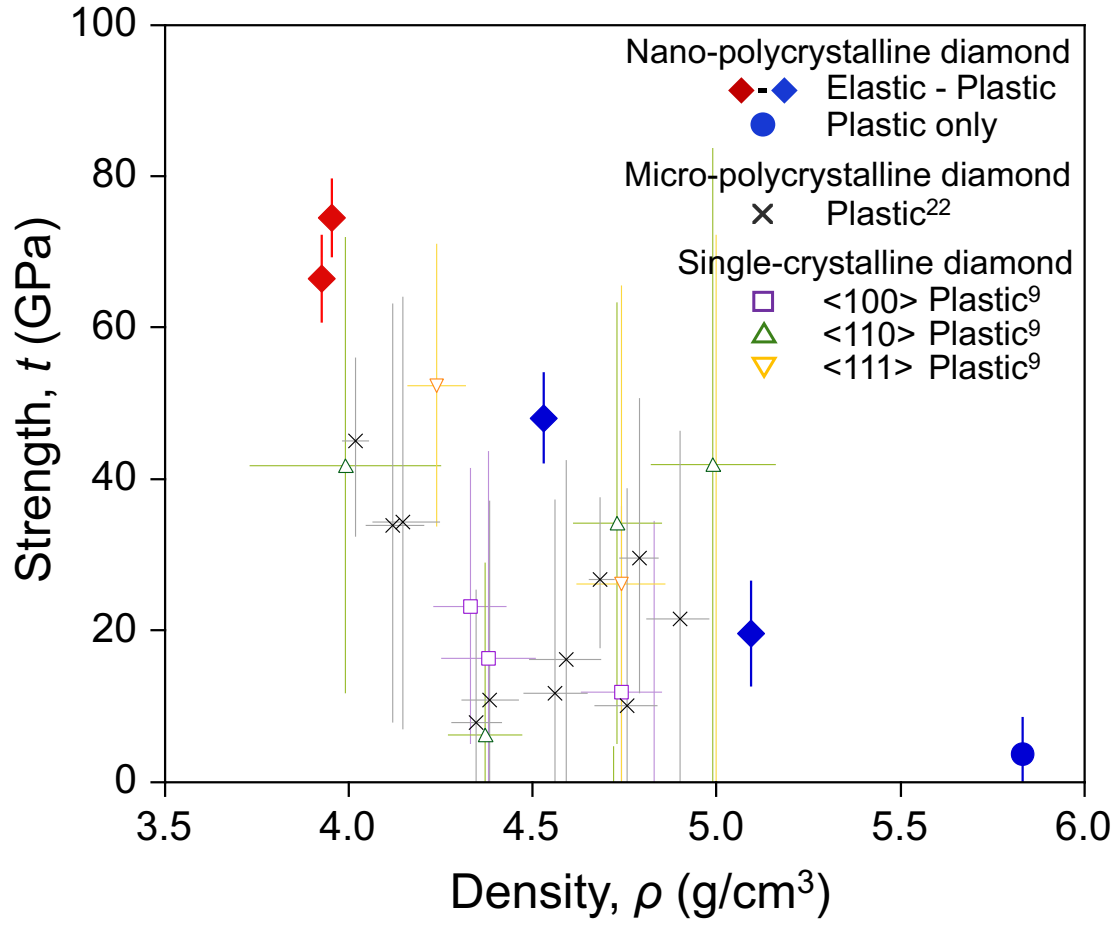


Fig. 4 | Strength of diamond under shock compression. Open symbols are the single-crystal diamond data from Ref. 9 with three different orientations: <100> (purple square), <110> (green triangle), and <111> (yellow reverse triangle). Other symbols and coloration are the same as in Fig. 3.

- Supplemental Material -

Strength of diamond beyond the elastic limit under dynamic compression

K. Katagiri^{1,2*}, N. Ozaki^{1,2}, L. E. Dresselhaus-Marais^{3,4}, J. H. Eggert³, Y. Inubushi^{5,6},
T. Irifune^{7,8}, M. Koenig^{1,9}, T. Matsuoka¹⁰, K. Miyanishi⁶, H. Nakamura¹,
N. Nishiyama¹¹, T. Okuchi¹², T. Sekine^{1,13}, Y. Seto¹⁴, K. Sueda⁶, Y. Tange⁵,
T. Togashi^{5,6}, Y. Umeda¹², M. Yabashi^{5,6}, T. Yabuuchi^{5,6}, and R. Kodama^{1,2}

¹Graduate School of Engineering, Osaka University, Osaka 565-0871, Japan.

²Institute of Laser Engineering, Osaka University, Osaka 565-0871, Japan.

³Lawrence Livermore National Laboratory; Livermore, CA 94550, USA.

⁴Department of MSE, Stanford University; Stanford, CA 94305, USA

⁵Japan Synchrotron Radiation Research Institute; Hyogo 679-5198, Japan.

⁶RIKEN SPring-8 Center; Hyogo 679-5148, Japan.

⁷Geodynamics Research Center, Ehime University; Ehime 790-0826, Japan.

⁸Earth-Life Science Institute, Tokyo Institute of Technology; Tokyo 145-0061, Japan.

⁹LULI, CNRS, CEA, École Polytechnique, UPMC, Univ Paris 06: Sorbonne
Universités, Institut Polytechnique de Paris; 91128 Palaiseau cedex, France.

¹⁰Open and Transdisciplinary Research Initiatives, Osaka University; Osaka 565-0871,
Japan.

¹¹Laboratory for Materials and Structures, Tokyo Institute of Technology; Kanagawa
226-8503, Japan.

¹²Institute for Integrated Radiation and Nuclear Science, Kyoto University; Osaka 590-
0494, Japan.

¹³Center for High-Pressure Science and Technology Advanced Research; Shanghai
201203, China.

¹⁴Graduate School of Science, Kobe University; Hyogo 657-0013, Japan.

*Corresponding author. Email: kkatagiri@ef.eie.eng.osaka-u.ac.jp

Estimation of temperature rise due to plastic work heating

The temperature increase due to plastic flow can be estimated from the measured strains of the diamond under shock [32-34]. The temperature increase due to plastic work is $\Delta T_{plastic} = \frac{f_{TQ}}{\rho_0 C_V} \int \sigma d\varepsilon_p$, where f_{TQ} is the Taylor-Quinney factor, C_V is the specific-heat at final pressure, ε_p is the plastic strain. The f_{TQ} of diamond is not well known but a recent ramp compression study of diamond [27] has observed the solid diamond phase at 2 TPa, suggesting f_{TQ} to be ~ 0.5 or even lower. We assumed $f_{TQ} = 0.5$ in presenting work though the Taylor-Quinney factor may depend on the grain size of the diamond and the strain rate of compression. The Dulong-Petit limit is used to estimate C_V , as the peak shock temperature in diamond should be higher than the Debye temperature at these shock pressures. The estimated temperature rises due to the plastic work at 262, 388, and 707 GPa are ~ 400 , ~ 1200 , and ~ 3100 K, respectively. Further investigations are needed to understand the effect of nano-grains on the plastic flow and associated heat generation.

The trend of the elastic stress with respect to the peak pressure

Previously published results of VISAR (velocity interferometer system for any reflector) [35] measurements of shock-compressed NPD showed that the longitudinal stress in the preceding elastic deformation is lower when the peak pressure is higher [13], in contrast to the data of the laser-shock experiments on single-crystal diamond with three different crystalline orientations which showed that the longitudinal stress in the preceding elastic deformation is higher when the peak pressure is higher [9]. The presenting XRD data of shock-compressed NPD showed a similar tendency with the VISAR measurements on NPD (Fig. S1).

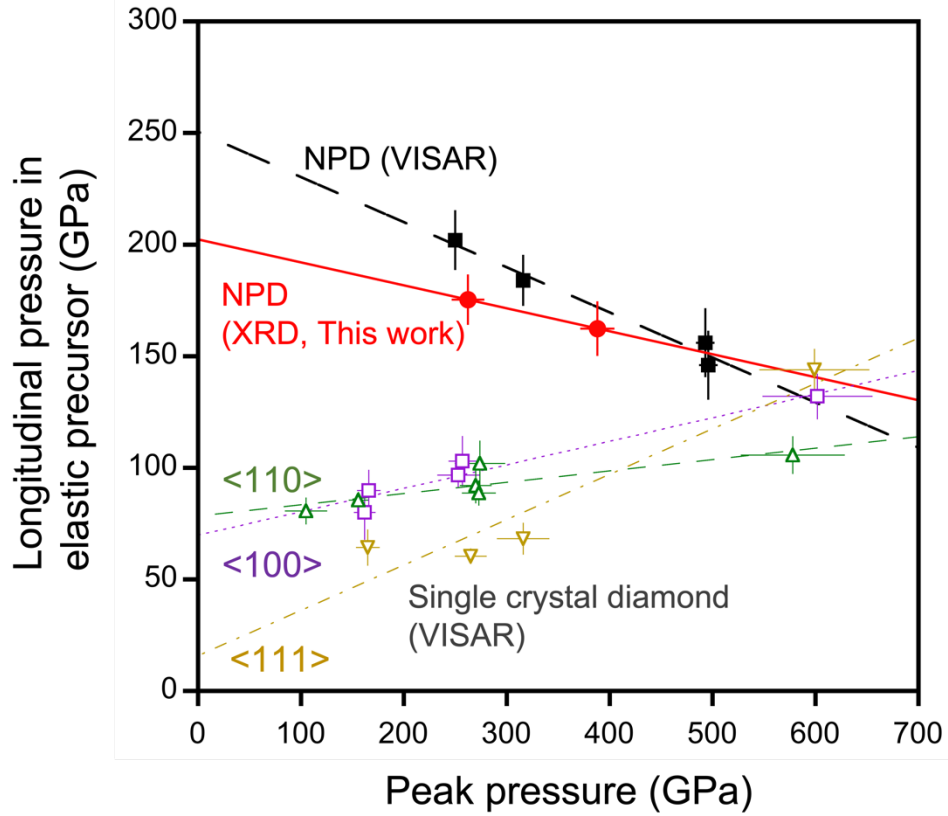


Fig. S1 | Longitudinal pressure in preceding elastic deformation (σ_x) versus the corresponding peak pressure (P_{max}) of diamond. Red filled circles and solid line are the data and its linear fit for the presenting XRD measurements. Other plots are previously reported VISAR results of NPD [13] (black filled square, long-dashed line) and single-crystal diamond with three different orientations [9]: $\langle 100 \rangle$ (purple open square, dotted line), $\langle 110 \rangle$ (green open triangle, dashed line), and $\langle 111 \rangle$ (yellow open reverse triangle, dot-dashed line).

Comparison of the strains determined by using diffraction peaks from different crystalline planes

For shot no. 79306 ($\sigma_x = 36$ GPa), the diffraction peaks from three different crystal planes of (111), (220), and (311) of elastically compressed volume are clearly recorded. Here, we determined normal and transverse strains from (111), (220), and (311) diffraction patterns individually. The results are shown in Fig. S2 and listed in Table S1. Only slight differences between these three diffraction peaks are confirmed, suggesting the high validity of the diffraction pattern prediction modeling [30] used in this work.

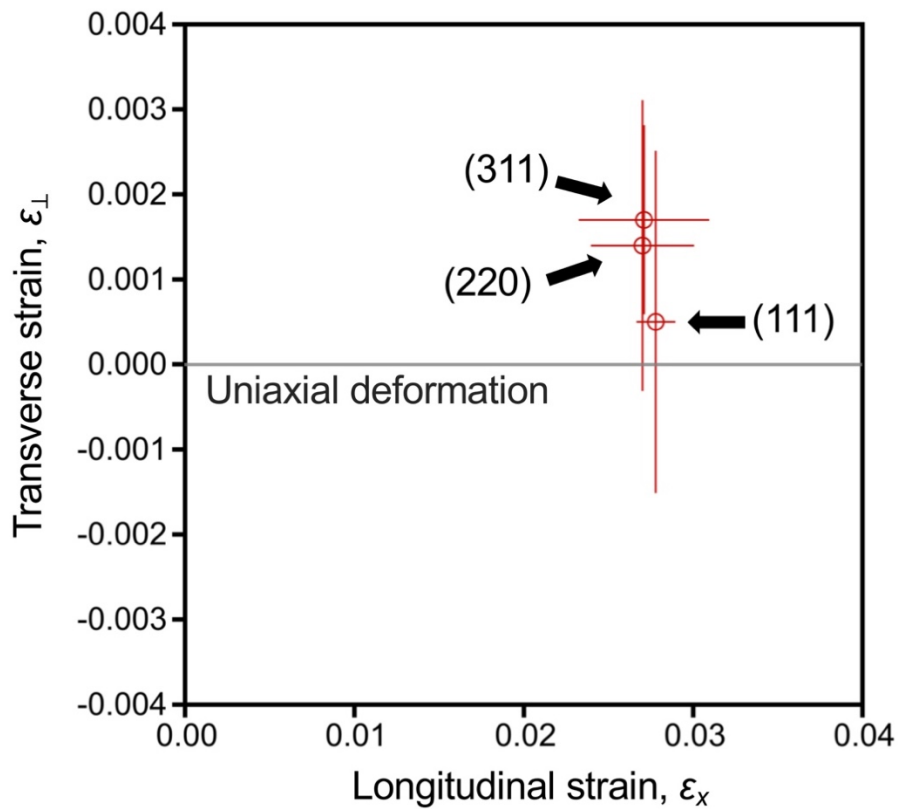


FIG. S2 | Comparison of shock normal and transverse strains determined from three diffraction peaks from three different crystal planes but the same shot (shot no. 79306).

Table S1. Comparison of shock normal and transverse strains determined from diffraction peaks from three different crystal planes but the same shot.

Shot number	Type of deformation	Crystal planes of diffraction	Shock normal direction ϕ_s (deg.)	Strain normal ϵ_n	Strain transverse ϵ_{\perp}	Density ρ (g/cm ³)	Pressure P (GPa)
796306	<i>elastic</i>	(111)	2.2	0.0278 ± 0.0011	0.0005 ± 0.0020	3.618 ± 0.011	36 ± 4
796306	<i>elastic</i>	(220)	2.2	0.0270 ± 0.0030	0.0014 ± 0.0017	3.622 ± 0.014	37 ± 4
796306	<i>elastic</i>	(311)	2.2	0.0271 ± 0.0038	0.0017 ± 0.0011	3.624 ± 0.015	38 ± 4

Summary of the x-ray diffraction data

Table S2 lists the normal strains, transverse strains, densities, pressures, and strengths determined from the recorded diffraction peaks. The normal strains listed in the main text, main figures, and Table S2 are determined from the lattice spacing of compressed (111) peaks observed at $\phi_S = 0$ degree. Different values of ϕ_S were observed between elastic and plastic deformations for the same shot. There are two possible explanations for this difference: one is that the elastic and plastic waves are propagating in different directions, and the other is that the plastic deformation is not actually uniaxial in the shock propagation direction but may involve shear terms.

The transverse strains listed in the main text, main figures, and Table S2 are determined by taking the weighted average of the transverse strain data obtained at different azimuthal angles [up to 18 data points taken at $\phi = \phi_S \pm 5n$ degrees (n is a positive integer from 1 to 9)] which are listed in Tables S3, S6-S11. Tables S4&5 list the data of shot no. 796306 obtained by diffractions from (220) and (311) planes, respectively. Figs. S3-S7 show the 1-dimensional XRD profiles for 5 shots presented in this work.

Table S2. Summary of the x-ray diffraction data.

Shot number	Type of deformation	Shock normal direction ϕ_s (deg.)	Strain normal ε_n	Strain transverse ε_\perp	Density ρ (g/cm ³)	Pressure P (GPa)	Strength t (GPa)
796306	<i>elastic</i>	2.2	0.0278 ± 0.0011	0.0005 ± 0.0020	3.618 ± 0.011	36 ± 4	—*
796308	<i>elastic</i>	3.1	0.0611 ± 0.0019	0.0031 ± 0.0039	3.766 ± 0.022	92 ± 8	—*
741076	<i>elastic</i>	-2.1	0.0848 ± 0.0017	0.0146 ± 0.0046	3.954 ± 0.027	175 ± 11	74.5 ± 5.2
741048	<i>elastic</i>	8.3	0.0776 ± 0.0019	0.0150 ± 0.0051	3.927 ± 0.030	162 ± 12	66.4 ± 5.8
741076	<i>plastic</i>	3.0	0.1073 ± 0.0048	0.0677 ± 0.0014	4.529 ± 0.026	262 ± 15	48.1 ± 6.1
741048	<i>plastic</i>	-15.2	0.1260 ± 0.0047	0.1116 ± 0.0020	5.094 ± 0.032	388 ± 16	19.6 ± 6.9
741052	<i>plastic</i>	0.8	0.1570 ± 0.0032	0.1546 ± 0.0005	5.832 ± 0.023	707 ± 8	3.67 ± 4.95

*Strength is not determined as the peak stress is below the Hugoniot elastic limit of NPD.

Table S3. Data of x-ray diffractions from (111) planes; Shot no. 796306 (Elastic).

$$\phi_s = 2.2 \text{ (deg.)}, \lambda = 1.127 \text{ (\AA)}, d_0 = 2.059 \text{ (\AA)}.$$

Azimuthal angle ϕ (deg.)	Scattering angle 2θ (deg.)	Lattice spacing d (\AA)	Strain normal ϵ_n	Strain transverse ϵ_{\perp}
$\phi_s + 45$	- ^a	-	-	-
$\phi_s + 40$	- ^a	-	-	-
$\phi_s + 35$	32.42 ± 0.17	2.019 ± 0.001	-	0.0018 ± 0.0487
$\phi_s + 30$	32.54 ± 0.21	2.013 ± 0.002	-	0.0084 ± 0.0590
$\phi_s + 25$	32.54 ± 0.21	2.009 ± 0.002	-	0.0021 ± 0.0674
$\phi_s + 20$	32.66 ± 0.22	2.004 ± 0.002	-	0.0180 ± 0.0874
$\phi_s + 15$	32.63 ± 0.25	2.006 ± 0.002	-	-0.0020 ± 0.1260
$\phi_s + 10$	32.67 ± 0.20	2.003 ± 0.002	-	0.0083 ± 0.1760
$\phi_s + 5$	32.67 ± 0.24	2.004 ± 0.002	-	-0.0334 ± 0.4250
$\phi_s \pm 0$	32.69 ± 0.28	2.002 ± 0.002	0.0278 ± 0.0011	-
$\phi_s - 5$	32.68 ± 0.23	2.005 ± 0.002	-	-0.0068 ± 0.4303
$\phi_s - 10$	32.67 ± 0.19	2.005 ± 0.002	-	0.0055 ± 0.1695
$\phi_s - 15$	32.59 ± 0.25	2.011 ± 0.002	-	-0.0172 ± 0.1269
$\phi_s - 20$	32.61 ± 0.23	2.010 ± 0.002	-	0.0062 ± 0.0888
$\phi_s - 25$	32.54 ± 0.28	2.013 ± 0.002	-	0.0014 ± 0.0796
$\phi_s - 30$	32.38 ± 0.26	2.021 ± 0.002	-	-0.0109 ± 0.0658
$\phi_s - 35$	32.28 ± 0.26	2.027 ± 0.002	-	-0.0111 ± 0.0598
$\phi_s - 40$	32.36 ± 0.26	2.022 ± 0.002	-	0.0022 ± 0.0562
$\phi_s - 45$	- ^a	-	-	-

^aCompressed peak could not be distinguished from the uncompressed peak.

Table S4. Data of x-ray diffractions from (220) planes; Shot no. 796306 (Elastic).

$$\phi_s = 2.2 \text{ (deg.)}, \lambda = 1.127 \text{ (\AA)}, d_0 = 1.261 \text{ (\AA)}.$$

Azimuthal angle ϕ (deg.)	Scattering angle 2θ (deg.)	Lattice spacing d (\AA)	Strain normal ϵ_n	Strain transverse ϵ_{\perp}
$\phi_s + 45$	- ^a	-	-	-
$\phi_s + 40$	54.13 ± 0.35	1.239 ± 0.003	-	0.0023 ± 0.0552
$\phi_s + 35$	54.27 ± 0.36	1.236 ± 0.003	-	0.0043 ± 0.0627
$\phi_s + 30$	54.39 ± 0.39	1.233 ± 0.003	-	0.0064 ± 0.0748
$\phi_s + 25$	54.52 ± 0.40	1.230 ± 0.003	-	0.0116 ± 0.0892
$\phi_s + 20$	54.60 ± 0.45	1.229 ± 0.004	-	0.0162 ± 0.1168
$\phi_s + 15$	54.57 ± 0.45	1.229 ± 0.003	-	0.0030 ± 0.1504
$\phi_s + 10$	54.65 ± 0.43	1.228 ± 0.003	-	0.0171 ± 0.2048
$\phi_s + 5$	54.67 ± 0.41	1.227 ± 0.003	-	0.0226 ± 0.2916
$\phi_s \pm 0$	54.68 ± 0.48	1.227 ± 0.004	0.0270 ± 0.0030	-
$\phi_s - 5$	54.65 ± 0.49	1.228 ± 0.004	-	0.0104 ± 0.3200
$\phi_s - 10$	54.53 ± 0.47	1.230 ± 0.004	-	-0.0308 ± 0.2124
$\phi_s - 15$	54.52 ± 0.45	1.230 ± 0.003	-	-0.0072 ± 0.1498
$\phi_s - 20$	54.38 ± 0.42	1.233 ± 0.003	-	-0.0151 ± 0.1120
$\phi_s - 25$	54.31 ± 0.42	1.235 ± 0.003	-	-0.0089 ± 0.0910
$\phi_s - 30$	54.32 ± 0.35	1.234 ± 0.003	-	0.0013 ± 0.0709
$\phi_s - 35$	54.13 ± 0.32	1.239 ± 0.002	-	-0.0037 ± 0.0592
$\phi_s - 40$	54.08 ± 0.36	1.240 ± 0.003	-	0.0001 ± 0.0561
$\phi_s - 45$	54.03 ± 0.34	1.241 ± 0.003	-	0.0029 ± 0.0504

^aPeak position is at outside of the detector.

Table S5. Data of x-ray diffractions from (311) planes; Shot no. 796306 (Elastic).

$$\phi_s = 2.2 \text{ (deg.)}, \lambda = 1.127 \text{ (\AA)}, d_0 = 1.076 \text{ (\AA)}.$$

Azimuthal angle ϕ (deg.)	Scattering angle 2θ (deg.)	Lattice spacing d (\AA)	Strain normal ϵ_n	Strain transverse ϵ_{\perp}
$\phi_s + 45$	- ^a	-	-	-
$\phi_s + 40$	- ^a	-	-	-
$\phi_s + 35$	64.56 ± 0.42	1.055 ± 0.003	-	0.0004 ± 0.0656
$\phi_s + 30$	64.75 ± 0.43	1.052 ± 0.003	-	0.0040 ± 0.0744
$\phi_s + 25$	64.83 ± 0.45	1.051 ± 0.003	-	0.0029 ± 0.0883
$\phi_s + 20$	64.89 ± 0.49	1.050 ± 0.004	-	0.0003 ± 0.1085
$\phi_s + 15$	65.01 ± 0.49	1.049 ± 0.004	-	0.0055 ± 0.1295
$\phi_s + 10$	65.10 ± 0.46	1.047 ± 0.003	-	0.0140 ± 0.1515
$\phi_s + 5$	65.11 ± 0.41	1.047 ± 0.003	-	0.0122 ± 0.1687
$\phi_s \pm 0$	65.17 ± 0.56	1.046 ± 0.004	0.0271 ± 0.0038	-
$\phi_s - 5$	65.13 ± 0.46	1.047 ± 0.003	-	0.0162 ± 0.1793
$\phi_s - 10$	65.08 ± 0.51	1.048 ± 0.004	-	0.0106 ± 0.1598
$\phi_s - 15$	65.05 ± 0.47	1.048 ± 0.003	-	0.0117 ± 0.1273
$\phi_s - 20$	64.87 ± 0.55	1.051 ± 0.004	-	-0.0018 ± 0.1154
$\phi_s - 25$	64.74 ± 0.53	1.053 ± 0.004	-	-0.0035 ± 0.0957
$\phi_s - 30$	64.67 ± 0.43	1.054 ± 0.003	-	-0.0001 ± 0.0744
$\phi_s - 35$	64.50 ± 0.41	1.056 ± 0.003	-	-0.0021 ± 0.0644
$\phi_s - 40$	64.43 ± 0.41	1.057 ± 0.003	-	0.0007 ± 0.0579
$\phi_s - 45$	64.29 ± 0.39	1.059 ± 0.003	-	0.0007 ± 0.0518

^aPeak position is at outside of the detector.

Table S6. Data of x-ray diffractions from (111) planes; Shot no. 796308 (Elastic).

$$\phi_s = 3.1 \text{ (deg.)}, \lambda = 1.127 \text{ (\AA)}, d_0 = 2.059 \text{ (\AA)}.$$

Azimuthal angle ϕ (deg.)	Scattering angle 2θ (deg.)	Lattice spacing d (\AA)	Strain normal ϵ_n	Strain transverse ϵ_{\perp}
$\phi_s + 45$	33.01 ± 0.39	1.983 ± 0.003	-	0.0095 ± 0.0654
$\phi_s + 40$	33.18 ± 0.47	1.974 ± 0.004	-	0.0105 ± 0.0752
$\phi_s + 35$	33.38 ± 0.44	1.962 ± 0.004	-	0.0159 ± 0.0776
$\phi_s + 30$	33.49 ± 0.48	1.956 ± 0.004	-	0.0148 ± 0.0907
$\phi_s + 25$	33.70 ± 0.44	1.944 ± 0.004	-	0.0310 ± 0.1006
$\phi_s + 20$	33.67 ± 0.50	1.946 ± 0.004	-	0.0080 ± 0.1374
$\phi_s + 15$	33.79 ± 0.43	1.939 ± 0.004	-	0.0192 ± 0.1764
$\phi_s + 10$	33.82 ± 0.49	1.937 ± 0.004	-	0.0069 ± 0.3246
$\phi_s + 5$	33.79 ± 0.40	1.939 ± 0.003	-	-0.1801 ± 0.6107
$\phi_s \pm 0$	33.89 ± 0.47	1.934 ± 0.004	0.0611 ± 0.0019	-
$\phi_s - 5$	33.83 ± 0.42	1.937 ± 0.003	-	-0.0808 ± 0.6786
$\phi_s - 10$	33.78 ± 0.41	1.939 ± 0.003	-	-0.0274 ± 0.2826
$\phi_s - 15$	33.61 ± 0.39	1.949 ± 0.003	-	-0.0505 ± 0.1635
$\phi_s - 20$	33.59 ± 0.40	1.950 ± 0.003	-	-0.0096 ± 0.1195
$\phi_s - 25$	33.40 ± 0.37	1.961 ± 0.003	-	-0.0169 ± 0.0922
$\phi_s - 30$	33.20 ± 0.39	1.973 ± 0.003	-	-0.0186 ± 0.0806
$\phi_s - 35$	33.27 ± 0.36	1.968 ± 0.003	-	0.0062 ± 0.0703
$\phi_s - 40$	33.03 ± 0.35	1.982 ± 0.002	-	0.0001 ± 0.0642
$\phi_s - 45$	32.90 ± 0.33	1.990 ± 0.003	-	0.0027 ± 0.0603

Table S7. Data of x-ray diffractions from (111) planes; Shot no. 741076 (Elastic).

 $\phi_s = -2.1$ (deg.), $\lambda = 1.240$ (Å), $d_0 = 2.059$ (Å).

Azimuthal angle ϕ (deg.)	Scattering angle 2θ (deg.)	Lattice spacing d (Å)	Strain normal ϵ_n	Strain transverse ϵ_{\perp}
$\phi_s + 45$	37.04 ± 0.51	1.952 ± 0.004	-	0.0145 ± 0.0711
$\phi_s + 40$	37.24 ± 0.46	1.942 ± 0.004	-	0.0121 ± 0.0709
$\phi_s + 35$	37.49 ± 0.55	1.929 ± 0.005	-	0.0137 ± 0.0838
$\phi_s + 30$	37.66 ± 0.39	1.921 ± 0.003	-	0.0087 ± 0.0792
$\phi_s + 25$	37.98 ± 0.48	1.906 ± 0.004	-	0.0233 ± 0.1040
$\phi_s + 20$	38.11 ± 0.41	1.899 ± 0.003	-	0.0211 ± 0.1208
$\phi_s + 15$	38.28 ± 0.35	1.891 ± 0.003	-	0.0339 ± 0.1521
$\phi_s + 10$	38.37 ± 0.40	1.887 ± 0.003	-	0.0506 ± 0.2810
$\phi_s + 5$	38.40 ± 0.46	1.885 ± 0.004	-	0.0396 ± 0.9060
$\phi_s \pm 0$	38.41 ± 0.43	1.885 ± 0.004	0.0848 ± 0.0017	-
$\phi_s - 5$	38.40 ± 0.41	1.885 ± 0.003	-	0.0555 ± 0.8383
$\phi_s - 10$	38.38 ± 0.46	1.886 ± 0.004	-	0.0605 ± 0.3108
$\phi_s - 15$	38.11 ± 0.45	1.899 ± 0.004	-	-0.0252 ± 0.1752
$\phi_s - 20$	37.99 ± 0.33	1.905 ± 0.003	-	-0.0040 ± 0.1065
$\phi_s - 25$	37.91 ± 0.42	1.909 ± 0.003	-	0.0141 ± 0.0966
$\phi_s - 30$	37.73 ± 0.33	1.918 ± 0.003	-	0.0156 ± 0.0730
$\phi_s - 35$	37.48 ± 0.46	1.930 ± 0.004	-	0.0126 ± 0.0767
$\phi_s - 40$	37.33 ± 0.50	1.937 ± 0.004	-	0.0181 ± 0.0744
$\phi_s - 45$	37.14 ± 0.39	1.947 ± 0.003	-	0.0194 ± 0.0622

Table S8. Data of x-ray diffractions from (111) planes; Shot no. 741048 (Elastic).

 $\phi_s = 8.3$ (deg.), $\lambda = 1.240$ (Å), $d_0 = 2.059$ (Å).

Azimuthal angle ϕ (deg.)	Scattering angle 2θ (deg.)	Lattice spacing d (Å)	Strain normal ϵ_n	Strain transverse ϵ_{\perp}
$\phi_s + 45$	37.06 ± 0.38	1.951 ± 0.003	-	0.0237 ± 0.0614
$\phi_s + 40$	37.21 ± 0.39	1.943 ± 0.003	-	0.0218 ± 0.0655
$\phi_s + 35$	37.66 ± 0.52	1.921 ± 0.004	-	0.0432 ± 0.0821
$\phi_s + 30$	37.67 ± 0.48	1.920 ± 0.004	-	0.0335 ± 0.0882
$\phi_s + 25$	37.87 ± 0.43	1.911 ± 0.004	-	0.0443 ± 0.9810
$\phi_s + 20$	37.79 ± 0.47	1.914 ± 0.004	-	0.0109 ± 0.1297
$\phi_s + 15$	38.00 ± 0.45	1.904 ± 0.004	-	0.0394 ± 0.1786
$\phi_s + 10$	38.07 ± 0.47	1.901 ± 0.004	-	0.0538 ± 0.3174
$\phi_s + 5$	38.10 ± 0.47	1.900 ± 0.004	-	0.0776 ± 0.9750
$\phi_s \pm 0$	38.10 ± 0.48	1.900 ± 0.004	0.0776 ± 0.0019	-
$\phi_s - 5$	38.05 ± 0.47	1.902 ± 0.004	-	-0.0797 ± 0.8597
$\phi_s - 10$	38.03 ± 0.44	1.903 ± 0.004	-	0.0151 ± 0.2972
$\phi_s - 15$	37.88 ± 0.44	1.910 ± 0.004	-	-0.0046 ± 0.1736
$\phi_s - 20$	37.59 ± 0.44	1.924 ± 0.004	-	-0.0316 ± 0.1247
$\phi_s - 25$	37.42 ± 0.43	1.933 ± 0.004	-	-0.0187 ± 0.0980
$\phi_s - 30$	37.25 ± 0.42	1.941 ± 0.003	-	-0.0093 ± 0.0823
$\phi_s - 35$	37.23 ± 0.41	1.942 ± 0.003	-	0.0097 ± 0.0725
$\phi_s - 40$	36.98 ± 0.40	1.955 ± 0.003	-	0.0072 ± 0.0663
$\phi_s - 45$	36.77 ± 0.38	1.966 ± 0.003	-	0.0085 ± 0.0615

Table S9. Data of x-ray diffractions from (111) planes; Shot no. 741076 (Plastic).

 $\phi_s = 3.0$ (deg.), $\lambda = 1.240$ (Å), $d_0 = 2.059$ (Å).

Azimuthal angle ϕ (deg.)	Scattering angle 2θ (deg.)	Lattice spacing d (Å)	Strain normal ϵ_n	Strain transverse ϵ_{\perp}
$\phi_s + 45$	38.68 ± 1.14	1.872 ± 0.009	-	0.0715 ± 0.1051
$\phi_s + 40$	38.65 ± 1.17	1.873 ± 0.010	-	0.0624 ± 0.1132
$\phi_s + 35$	38.88 ± 1.15	1.863 ± 0.009	-	0.0678 ± 0.1227
$\phi_s + 30$	39.12 ± 1.17	1.852 ± 0.010	-	0.0779 ± 0.1412
$\phi_s + 25$	39.15 ± 1.19	1.850 ± 0.010	-	0.0713 ± 0.1724
$\phi_s + 20$	39.23 ± 1.18	1.847 ± 0.010	-	0.0688 ± 0.2242
$\phi_s + 15$	39.32 ± 1.18	1.843 ± 0.010	-	0.0717 ± 0.3308
$\phi_s + 10$	39.36 ± 1.23	1.841 ± 0.010	-	0.0604 ± 0.6339
$\phi_s + 5$	39.38 ± 1.29	1.840 ± 0.011	-	-0.0050 ± 2.1397
$\phi_s \pm 0$	39.42 ± 1.20	1.838 ± 0.010	0.1073 ± 0.0048	-
$\phi_s - 5$	39.41 ± 1.18	1.839 ± 0.010	-	0.0788 ± 2.1332
$\phi_s - 10$	39.35 ± 1.17	1.841 ± 0.010	-	0.0556 ± 0.6080
$\phi_s - 15$	39.26 ± 1.19	1.846 ± 0.010	-	0.0499 ± 0.3305
$\phi_s - 20$	39.26 ± 1.17	1.845 ± 0.010	-	0.0753 ± 0.2232
$\phi_s - 25$	39.03 ± 1.21	1.856 ± 0.010	-	0.0548 ± 0.1736
$\phi_s - 30$	39.00 ± 1.19	1.857 ± 0.010	-	0.0669 ± 0.1426
$\phi_s - 35$	38.79 ± 1.21	1.867 ± 0.010	-	0.0609 ± 0.1263
$\phi_s - 40$	38.77 ± 1.20	1.868 ± 0.010	-	0.0694 ± 0.1147
$\phi_s - 45$	38.65 ± 1.17	1.874 ± 0.010	-	0.0700 ± 0.1063

Table S10. Data of x-ray diffractions from (111) planes; Shot no. 741048 (Plastic).

 $\phi_s = -15.2$ (deg.), $\lambda = 1.240$ (Å), $d_0 = 2.059$ (Å).

Azimuthal angle ϕ (deg.)	Scattering angle 2θ (deg.)	Lattice spacing d (Å)	Strain normal ϵ_n	Strain transverse ϵ_{\perp}
$\phi_s + 45$	39.97 ± 1.19	1.814 ± 0.010	-	0.1108 ± 0.1056
$\phi_s + 40$	40.00 ± 1.17	1.813 ± 0.010	-	0.1093 ± 0.1120
$\phi_s + 35$	40.18 ± 1.16	1.805 ± 0.010	-	0.1177 ± 0.1225
$\phi_s + 30$	40.15 ± 1.18	1.806 ± 0.010	-	0.1123 ± 0.1411
$\phi_s + 25$	40.21 ± 1.17	1.804 ± 0.010	-	0.1145 ± 0.1698
$\phi_s + 20$	40.20 ± 1.16	1.804 ± 0.010	-	0.1065 ± 0.2200
$\phi_s + 15$	40.24 ± 1.13	1.802 ± 0.009	-	0.1059 ± 0.3165
$\phi_s + 10$	40.21 ± 1.13	1.804 ± 0.009	-	0.0598 ± 0.5707
$\phi_s + 5$	40.27 ± 1.18	1.801 ± 0.010	-	0.0493 ± 1.9621
$\phi_s \pm 0$	40.30 ± 1.18	1.800 ± 0.010	0.1260 ± 0.0047	-
$\phi_s - 5$	40.24 ± 1.23	1.802 ± 0.010	-	-0.0249 ± 1.9621
$\phi_s - 10$	40.24 ± 1.22	1.802 ± 0.010	-	0.0849 ± 0.6124
$\phi_s - 15$	40.28 ± 1.20	1.801 ± 0.010	-	0.1194 ± 0.3320
$\phi_s - 20$	40.29 ± 1.09	1.800 ± 0.009	-	0.1244 ± 0.2126
$\phi_s - 25$	40.24 ± 1.10	1.802 ± 0.009	-	0.1184 ± 0.1640
$\phi_s - 30$	40.19 ± 1.10	1.805 ± 0.009	-	0.1159 ± 0.1356
$\phi_s - 35$	39.95 ± 1.16	1.815 ± 0.010	-	0.1014 ± 0.1224
$\phi_s - 40$	- ^a	-	-	-
$\phi_s - 45$	- ^a	-	-	-

^aPeak position is at outside of the detector.

Table S11. Data of x-ray diffractions from (111) planes; Shot no. 741052 (Plastic).

 $\phi_s = 0.8$ (deg.), $\lambda = 1.240$ (Å), $d_0 = 2.059$ (Å).

Azimuthal angle ϕ (deg.)	Scattering angle 2θ (deg.)	Lattice spacing d (Å)	Strain normal ϵ_n	Strain transverse ϵ_{\perp}
$\phi_s + 45$	41.81 ± 0.77	1.738 ± 0.006	-	0.1553 ± 0.0832
$\phi_s + 40$	41.80 ± 0.74	1.738 ± 0.006	-	0.1544 ± 0.0870
$\phi_s + 35$	41.84 ± 0.75	1.736 ± 0.006	-	0.1564 ± 0.0961
$\phi_s + 30$	41.85 ± 0.76	1.736 ± 0.006	-	0.1570 ± 0.1102
$\phi_s + 25$	41.80 ± 0.77	1.736 ± 0.006	-	0.1510 ± 0.1326
$\phi_s + 20$	41.85 ± 0.76	1.736 ± 0.006	-	0.1570 ± 0.1683
$\phi_s + 15$	41.81 ± 0.79	1.736 ± 0.006	-	0.1441 ± 0.2438
$\phi_s + 10$	41.84 ± 0.79	1.736 ± 0.006	-	0.1499 ± 0.4275
$\phi_s + 5$	41.85 ± 0.80	1.736 ± 0.007	-	0.1570 ± 1.3338
$\phi_s \pm 0$	41.85 ± 0.81	1.736 ± 0.007	0.1570 ± 0.0032	-
$\phi_s - 5$	41.85 ± 0.79	1.736 ± 0.006	-	0.1570 ± 1.3199
$\phi_s - 10$	41.84 ± 0.78	1.736 ± 0.006	-	0.1499 ± 0.4237
$\phi_s - 15$	41.83 ± 0.76	1.737 ± 0.006	-	0.1506 ± 0.2385
$\phi_s - 20$	41.85 ± 0.74	1.737 ± 0.006	-	0.1570 ± 0.1657
$\phi_s - 25$	41.82 ± 0.75	1.737 ± 0.006	-	0.1534 ± 0.1307
$\phi_s - 30$	41.79 ± 0.74	1.738 ± 0.006	-	0.1518 ± 0.1087
$\phi_s - 35$	41.83 ± 0.74	1.738 ± 0.006	-	0.1557 ± 0.0955
$\phi_s - 40$	41.80 ± 0.75	1.738 ± 0.006	-	0.1544 ± 0.0876
$\phi_s - 45$	41.80 ± 0.73	1.739 ± 0.006	-	0.1549 ± 0.0809

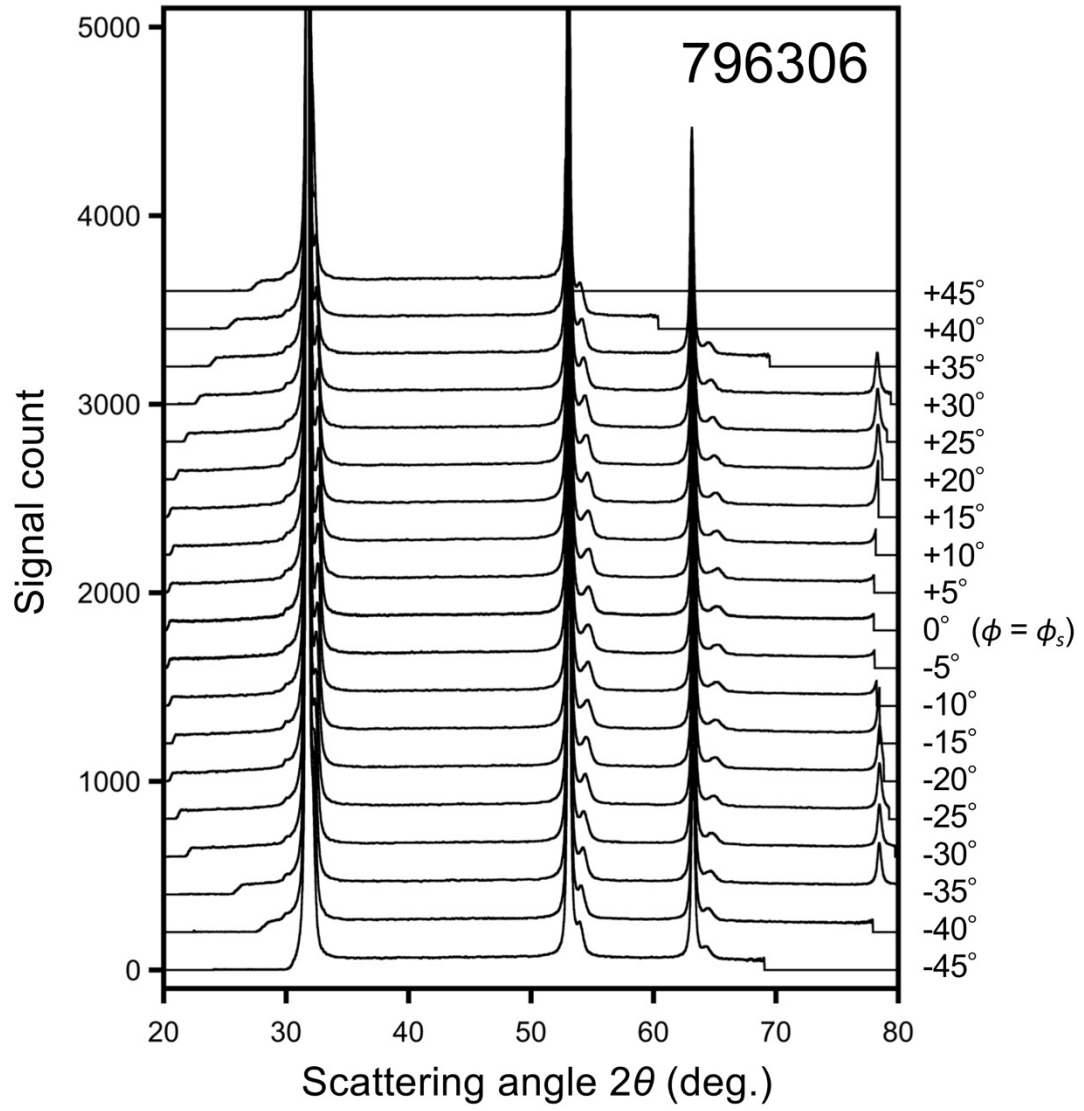


Fig. S3 | X-ray diffraction profiles showing pure elastic deformation with peak pressure of 36 GPa. Shot no. 796306. $\phi_s = 2.2$ (deg.), $\lambda = 1.127$ (Å).

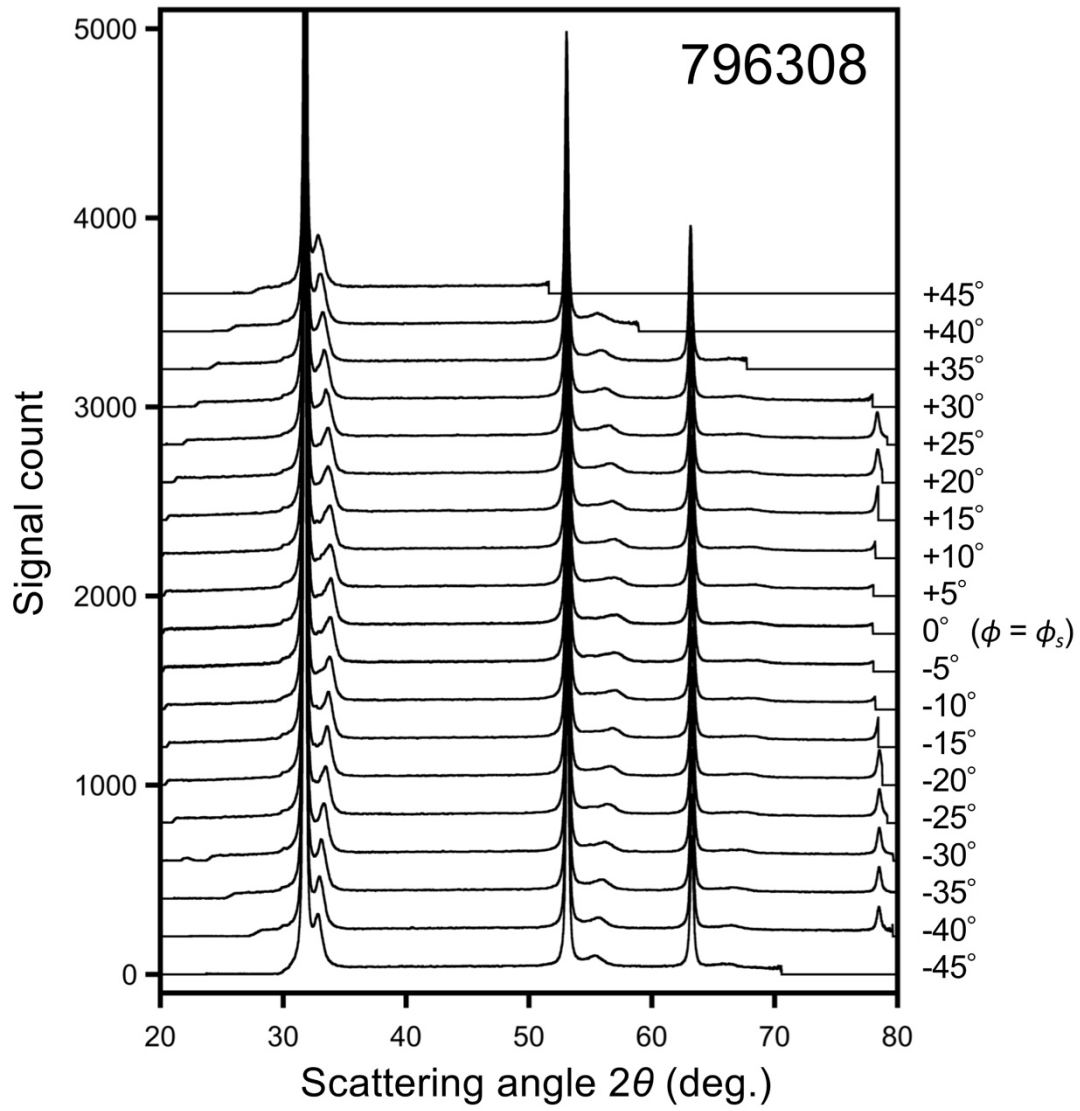


Fig. S4 | X-ray diffraction profiles showing pure elastic deformation with peak pressure of 92 GPa. Shot no. 796308. $\phi_s = 3.1$ (deg.), $\lambda = 1.127$ (Å).

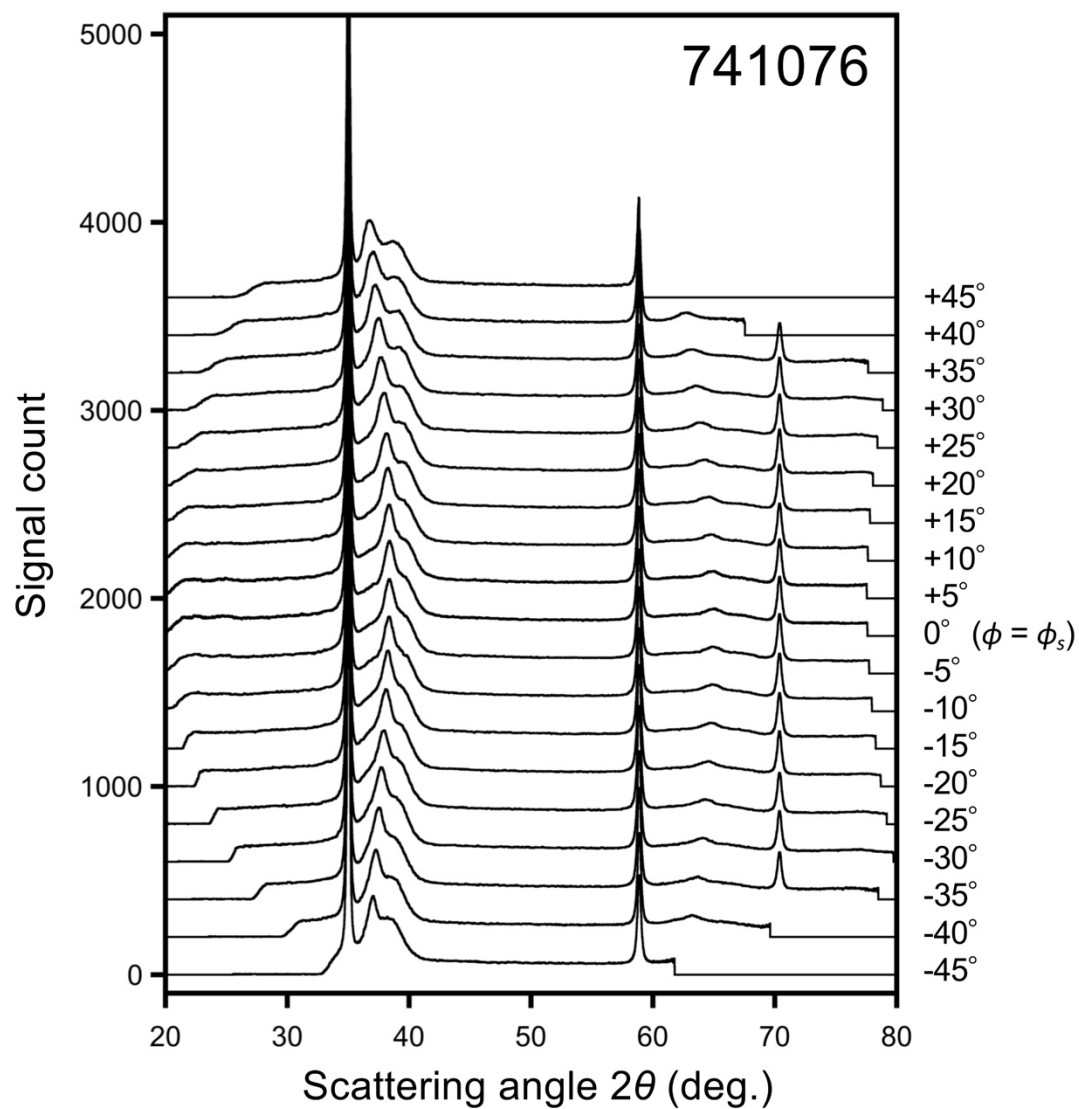


Fig. S5 | X-ray diffraction profiles showing elastic-plastic two-wave structure with peak pressure of 262 GPa. Shot no. 741076. $\phi_s = -2.1$ (deg.), $\lambda = 1.240$ (Å).

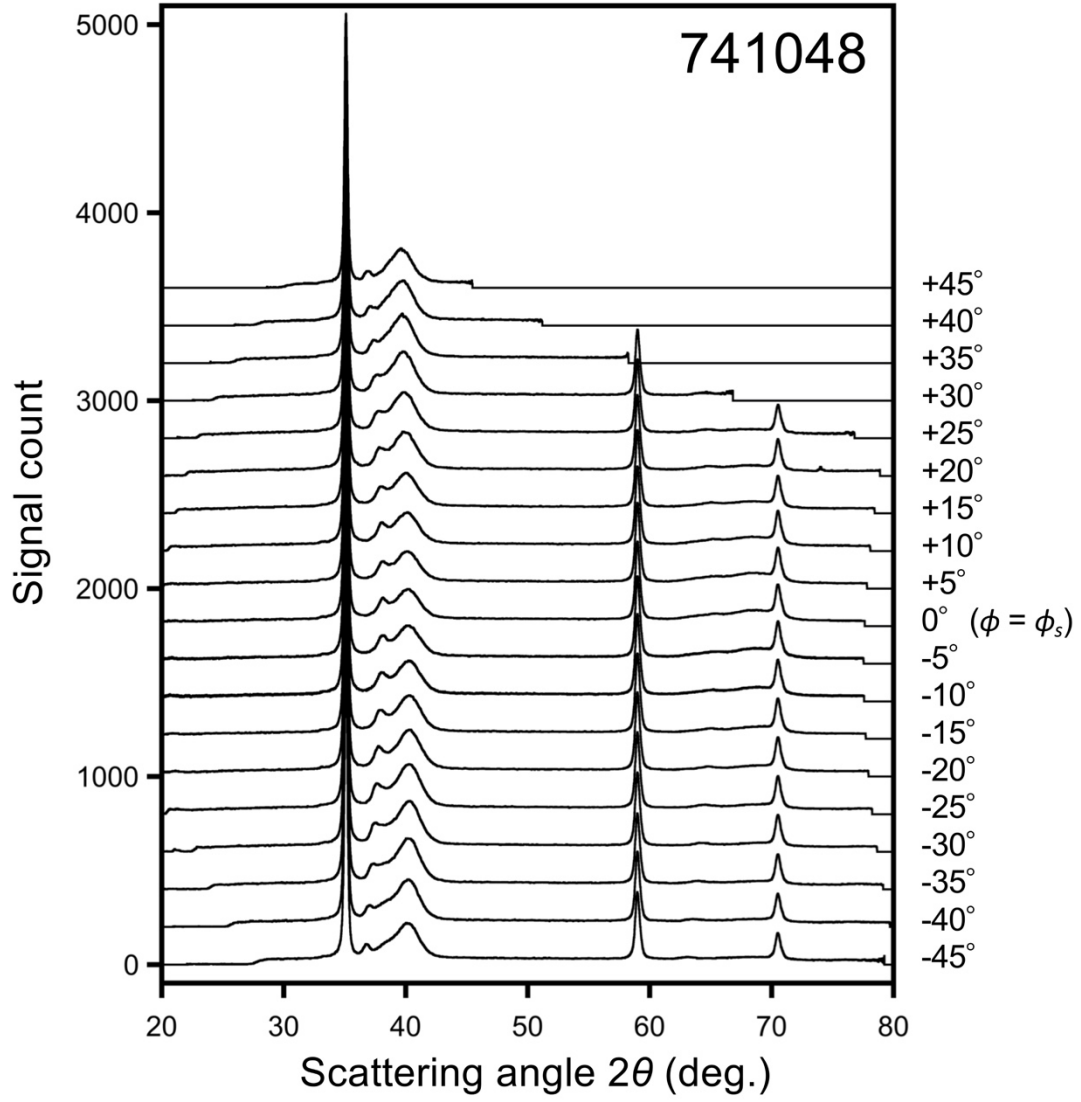


Fig. S6 | X-ray diffraction profiles showing elastic-plastic two-wave structure with peak pressure of 388 GPa. Shot no. 741048. $\phi_s = 8.3$ (deg.), $\lambda = 1.240$ (Å).

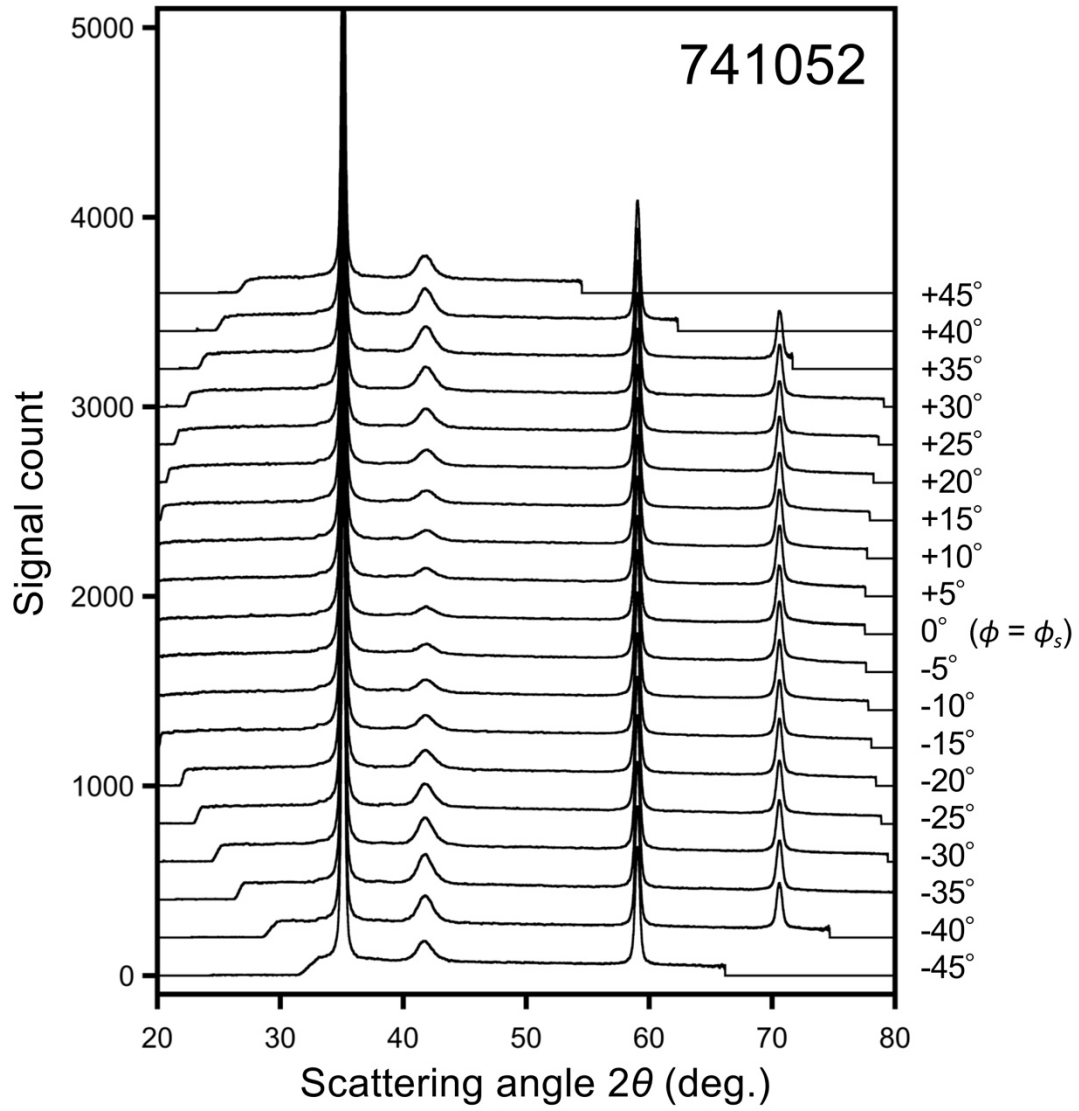


Fig. S7 | X-ray diffraction profiles showing plastic deformation with peak pressure of 707 GPa. Elastic wave is overdriven. Shot no. 741052. $\phi_s = 0.8$ (deg.), $\lambda = 1.240$ (Å).

XRD peak fitting

In most cases, recorded diffraction peaks were fitted by using multiple gaussian shapes. For the data of shot no. 741076, however, the stress gradient in the plastically deformed volume is ineligious and a split-gaussian (same height but different width between the left half and the right half) was used to take the fit (the blue solid profile in Fig. S8). The uncertainties were determined from the full-width at half-maximum of the gaussian fit, even when the split-gaussian was applied (to evaluate only the peak compression state).

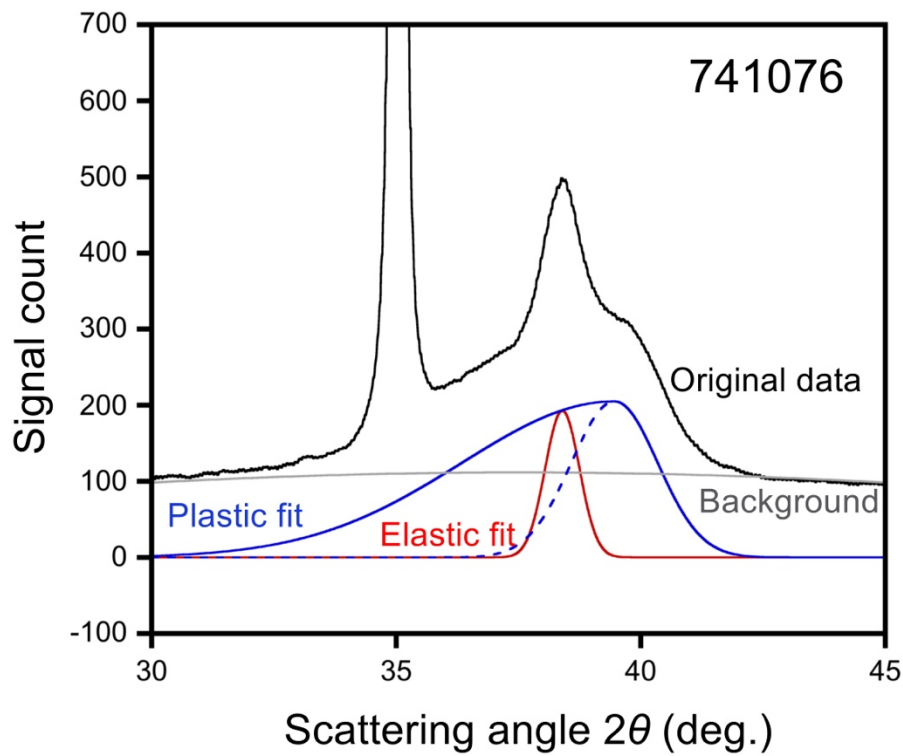


Fig. S8 | Example of the XRD peak fitting (shot no. 741076; $\phi = \phi_s$). The uncompressed peak at $2\theta = 34 - 36$ degrees was masked prior to the fitting.

References

1. Meyers, M. A. *Dynamic behavior of materials* (Wiley, New York, 1994).
2. Johnson, Q., Mitchell, A. & Evans, L. X-ray diffraction evidence for crystalline order and isotropic compression during the shock-wave process. *Nature* **231**, 310-311 (1971).
3. Zhakhovsky, V. V., Budzevich, M. M., Inogamov, N. A., Oleynik, I. I. & White, C. T. Two-zone elastic-plastic single shock waves in solids. *Phys. Rev. Lett.* **107**, 135502 (2011).
4. Bringa, E. M. et al. Ultrahigh strength in nanocrystalline materials under shock loading. *Science* **309**, 1838 (2005).
5. McWilliams, R. S. et al. Phase transformations and metallization of magnesium oxide at high pressure and temperature. *Science* **338**, 1330-1333 (2012).
6. Millot, M. et al., Shock compression of stishovite and melting of silica at planetary interior conditions. *Science* **347**, 418-420 (2015).
7. Knudson, M. D., Desjarlais, M. P. & Dolan, D. H. Shock wave exploration of the high-pressure phases of carbon. *Science* **322**, 1822 (2008).
8. Smith, R.F. et al., Ramp compression of diamond to five terapascals. *Nature*, **511**, 330-333 (2014).
9. McWilliams, R. S. et al. Strength effects in diamond under shock compression from 0.1 to 1 TPa. *Phys. Rev. B* **81**, 014111 (2010).
10. Meyers, M. A. & Chawla, K. K. *Mechanical behavior of materials* (Prentice-Hall, Upper Saddle River, NJ, 1999).
11. Madec, R. et al., The role of collinear interaction in dislocation-induced hardening. *Science* **301**, 1879 (2003).
12. Irifune, T. et al. Ultrahard polycrystalline diamond from graphite. *Nature* **421**, 599-600 (2003).
13. Katagiri, K. et al. Shock response of full density nanopolycrystalline diamond. *Phys. Rev. Lett.* **125**, 185701 (2020).
14. Ishikawa, T. et al. A compact X-ray free-electron laser emitting in the sub-ångström region. *Nat. Photonics* **22**, 540-544 (2012).
15. Swift, D. C., Tierney IV, T. E., Kopp, R. A. & Gammel, J. T. Shock pressures induced in condensed matter by laser ablation. *Phys. Rev. E* **69**, 036406 (2004).
16. Inubushi, Y. et al. Development of an experimental platform for combinative use of an XFEL and a high-power nanosecond laser. *Appl. Sci.* **10**, 2224 (2020).
17. Chang, Y. -Y., Jacobson, S. D., Kimura, M., Irifune, T. & Ohno, I. Elastic properties of transparent nano-polycrystalline diamond measured by GHz-ultrasonic

- interferometry and resonant sphere methods. *Phys. Earth Planet. Inter.* **228**, 47 (2014).
18. Eggert, J. H., Weck, G., Loubeyre, P. & Mezouar, M. Quantitative structure factor and density measurements of high-pressure fluids in diamond anvil cells by x-ray diffraction: Argon and water. *Phys. Rev. B* **65**, 174105 (2002).
 19. MacDonald, M. J. et al. Calculation of Debye-Scherrer diffraction patterns from highly stressed polycrystalline materials. *J. Appl. Phys.* **119**, 215902 (2016).
 20. MacDonald, M. J. et al. Using simultaneous x-ray diffraction and velocity interferometry to determine material strength in shock-compressed diamond. *Appl. Phys. Lett.* **116**, 23104 (2020).
 21. Kocks, U. F., Tomé, C. N. & Wenk, H.-R. *Texture and anisotropy: preferred orientations in polycrystals and their effect on materials properties* (Cambridge Univ. Press, New York, 1998).
 22. Margulies, L., Winther, G. & Poulsen, H. F. In situ measurement of grain rotation during deformation of polycrystals. *Science* **291**, 2392 (2001).
 23. Grady, D. E. Shock deformation of brittle solids. *J. Geophys. Res.* **85**, 913-924 (1980).
 24. Graham, R. A. & Brooks, W. P. Shock-wave compression of sapphire from 15 to 420 kbar. The effects of large anisotropic compressions. *J. Phys. Chem. Solids*, **32**, 2311-2330 (1971).
 25. Bavdekar, S. & Subhash, G. Comparison of pressure-sensitive strength models for ceramics under ultrahigh confinement. *Int. J. Impact Eng.* **118**, 60-66 (2018).
 26. Kanel, G. I., Razorenov, S. V., & Fortov, E. *Shock-wave phenomena and the properties of condensed matter* (Springer-Verlag, New York, 2004).
 27. Lazicki, A. et al., Metastability of diamond ramp-compressed to 2 terapascals. *Nature* **589**, 532-535 (2021).
 28. Park, H.-S. et al., Techniques for studying materials under extreme states of high energy density compression. *Phys. Plasmas* **28**, 060901 (2021).
 29. Katagiri, K. et al. Optical properties of shock-compressed diamond up to 550 GPa. *Phys. Rev. B* **101**, 184106 (2020).
 30. Higginbotham, A. & McGonegle, D. Prediction of Debye-Scherrer diffraction patterns in arbitrarily strained samples. *J. Appl. Phys.* **115**, 174906 (2014).
 31. Singh, A. K., The lattice strains in a specimen (cubic system) compressed nonhydrostatically in an opposed anvil device. *J. Appl. Phys.* **73**, 4278 (1993).
 32. Bradley, D. K. et al. Diamond at 800 GPa. *Phys. Rev. Lett.* **102**, 075503 (2009).

33. Ping, Y. et al. Solid iron compressed up to 560 GPa. *Phys. Rev. Lett.* **111**, 065501 (2013).
34. Heighway, P. G. et al. Nonisentropic release of a shocked solid. *Phys. Rev. Lett.* **123**, 245501 (2019).
35. Celliers, P. M., Bradley, D. K., Collins, G. W. & Hicks D. G. Line-imaging velocimeter for shock diagnostics at the OMEGA laser facility. *Rev. Sci. Instrum.* **75**, 4916 (2004).